RSC Advances

ROYAL SOCIETY OF CHEMISTRY

www.rsc.org/advances

Journal Name

RSCPublishing

ARTICLE

Digitization of Two-Phase Flow Patterns in a Microchannel Induced by an External AC Field

Cite this: DOI: 10.1039/xoxxoooooox

Abhinav Sharma,[a] Joydip Chaudhuri,[a] Vineet Kumar,[a] Seim Timung,[a] Tapas Kumar Mandal[a,b] and Dipankar Bandyopadhyay*[a,b]

Received ooth February 2015,
Accepted ooth xxxxxxxxxxxx

DOI: 10.1039/xoxxoooooox

www.rsc.org/

Externally applied alternating current (AC) electrostatic field can deform the interface of a pair of weakly conducting liquids to engender droplet flow patterns inside the 'T' shaped microchannels. The electrohydrodynamic stresses originating from the accumulation of free and induced charges at the interface of the immiscible liquids stimulate the formation of droplets with higher surface to volume ratio. Strikingly, the size, shape, and frequency of the flow patterns can be tuned by varying the frequency and waveform of the external AC field. The enhanced dielectrophoretic force at a higher field intensity and lower frequency of the AC field facilitates the formation of droplets with smaller size and higher throughput. The size, shape, and frequency of the droplets are also found to be functions of the ratio of the electrical conductivity of the phases and the interfacial tension. The proposed methodology demonstrates a non-invasive pathway to digitize the flow patterns inside a multiphase microfluidic device with the help of an external AC field.

1. Introduction

Programmable digital microfluidics is poised to be the next tipping point for diverse technological processes which include the bio-analysis tools,[1,2] MEMS devices,[3-5] microfluidic systems,[6-8] microreactors,[9,10] and advanced theragnostic devices.[11-16] This is because, the discrete droplet flow patterns brings in the unique advantages in, ultra-fast response time owing to a higher throughput, availability of larger surface to volume ratio for the energy, momentum and mass transfer, superior control over the processes, and opening up the possibility of multi-tasking.[17-22] The scientific aspects owing to the complex interplay between the dominant capillary and frictional forces over the dormant inertial and gravitational forces at the microscale have also attracted attention over the years.[23-28] Based on these factors, a number of intriguing phenomena have been unveiled which include the synthesis of micro-dispersions,[29,30] fabrication of large-area interfacial micropatterns,[31-33] formation of liquid vesicles for transport and reaction,[34] rapid mixing at the microscale[35] and microreactor technologies for particle synthesis.[36] The present focus is directed towards the integration of the special features of the digital microfluidics into the next-generation commercial devices to improve the efficiency of the processes.[37-42]

The digitization of the flow patterns by forming bubbles or droplets of the conventional pressure-driven gas-liquid[43-48] or liquid-liquid[49-52] flows inside the microchannels has been investigated extensively over the past few decades. Recent studies indicate that, the use of external field can be another effective alternative to stimulate the flow patterns suitable for digital microfluidics.[53-59] The external field can disrupt the regular interplay between the capillary, inertial, gravitational, and viscous forces in a microscale pressure-driven slug or plug or stratified flow to produce droplets.[60-71] The non-invasive nature enables facile integration of this method with the existing commercial devices without hindering the basic design of the process.

The theoretical modeling of the dynamics of the multiphase flows under the influence of an external electric field is also a very challenging area of research because of the complexities associated with the development of the 'interface-tracking' methodologies. A number of recent works have shown that the Poisson's equation for the electric field coupled with the Stokes equation for the flow can be solved numerically to analyze the experimental results on the electrohydrodynamic (EHD) breakup of droplets at the microscale.[60,64] The electric field induced deformation of the drops having leaky dielectric, perfectly dielectric, and constant charge properties have also been investigated numerically employing the finite element or finite volume techniques coupled with the volume-of-fluid (VOF) or level-set (CLSVOF) method.[65-68] Lattice-Boltzmann method (LBM) is also employed to solve the entire system of

transport equations for the two-phase systems.[69] Recent studies reveal that the phase-field method can be another efficient alternative to study these systems because it is computationally less intensive while tracking the spatiotemporally evolution of the deforming interfaces of the two-phase flows.[71-78]
However, most of the previous studies focus on the electric field induced deformation of different two-phase stationary configurations like droplets, slugs, or plugs. The studies related to the influence of the external electrostatic field on the evolving interfacial morphologies have received far less attention.[62,70] A very recent experimental study[7] have shown the pathways to generate droplets inside a flow-focusing microchannel setup with the help of the non-invasive alternating current (AC) electric field. Subsequently, a computational work have demonstrated the strategies to disintegrate the pressure-driven flow patterns into droplets with the help of a localized direct current (DC) external electric field.[79]

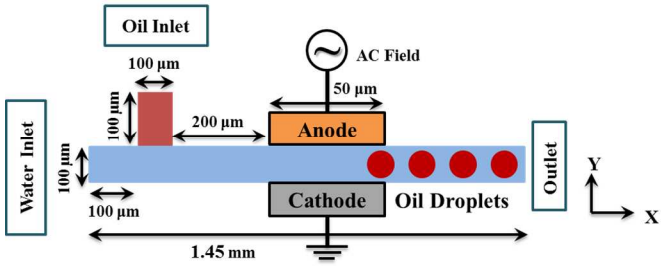

Figure 1. Schematic diagram of the 'T' shaped microchannel. The alternating current (AC) electric field is generated through the electrodes (anode and cathode), placed 0.2 mm downstream from the T-junction of the channel. The channel diameter d_c = 0.1 mm, which is same as the electrode separation distance.

The present study shows a simple method to generate droplets from an oil-water microflow with the help of an AC electric field. **Figure 1** schematically shows that when a localized AC field is generated in the downstream of a 'T' junction microchannel, the regular pressure-driven oil-water flow patterns can transform into droplets. The variation in the dielectrophoretic force at the interface of the phases with the variation in the strength of the AC field helps in the digitization of the flow patterns. Example situations are shown where a pressure-driven stratified flow is converted into droplets by tuning the frequency of the AC field, conductivity ratio of the phases, and the interfacial tension. Remarkably, even the waveform of the AC field is found to have a very strong influence on the droplet generation and their miniaturization. The proposed methodology shows a pathway to non-invasively control the surface to volume ratio and throughput of the flow patterns with the help of a localized electric field inside a microfluidic device.

2. Problem Formulation

2.1 Governing Equations and Boundary Conditions

The flow of a pair of incompressible, immiscible and Newtonian liquids inside a microchannel are governed by the following continuity and equations of motion,

$$\nabla \cdot \mathbf{u}_i = 0, \quad (1)$$

$$\rho(\dot{\mathbf{u}}_i + \mathbf{u}_i \cdot \nabla \mathbf{u}_i) = -\nabla p_i + \nabla \cdot (\boldsymbol{\tau}_i + \mathbf{M}_i) + \mathbf{f}_{st} + \rho \mathbf{g}. \quad (2)$$

In the equations, (1) and (2) the subscript 'i' corresponds to oil (i = 1) and water (i = 2) phases. The notation $\mathbf{u}_i$ denotes the velocity vector, η_i is dynamic viscosity, ρ_i is density, p_i is the pressure of the i^{th} liquid. The symbol over dot denotes the time derivative and the vector $\mathbf{g}$ is the acceleration due to gravity acting on the negative y direction for the geometry shown in the **Figure 1**. The Newtonian stress tensor for the hydrodynamic field is defined as, $\boldsymbol{\tau}_i = \eta_i[\nabla \mathbf{u}_i + \nabla \mathbf{u}_i^T]$ and the Maxwell's stresses for the electric field is defined by the tensor, $\mathbf{M}_i = \varepsilon_0 \varepsilon_i [\mathbf{E}_i \otimes \mathbf{E}_i - 0.5(\mathbf{E}_i \cdot \mathbf{E}_i)\mathbf{I}]$. The surface tension force is defined as, $\mathbf{f}_{st} = G\nabla\phi$, a product of the chemical potential (G) and the gradient of the phase field (ϕ), which is defined in the following section.
In the absence of magnetic field, the irrotational ($\nabla \times \mathbf{E}_i = 0$) electric field ($\mathbf{E}_i$) applied across the channel can be expressed in terms of the potential function (V_i) as, $\mathbf{E}_i = -\nabla V_i$. Replacing this relation in the Gauss's law for the purely dielectric ($\nabla \cdot \varepsilon_i \mathbf{E}_i = 0$) and the leaky dielectric ($\nabla \cdot \sigma_i \mathbf{E}_i = 0$) leads to the Laplace equation for the i^{th} fluid as, $\nabla^2 V_i = 0$, where ε_i is the dielectric constant and σ_i is the conductivity of the i^{th} phase. For purely dielectric fluids, the electrostatic force acting on the i^{th} fluid is represented as,

$$f_V^d = \nabla \cdot \mathbf{M}_i = -\frac{1}{2}\varepsilon_0 \mathbf{E}_i^2 \nabla \varepsilon \,. \quad (3)$$

For the leaky dielectric fluids, the electrostatic force acting on the i^{th} fluid can be estimated from the divergence of the Maxwell's stress tensor as,

$$f_V^c = \nabla \cdot \mathbf{M}_i = -\frac{1}{2}\varepsilon_0 \mathbf{E}_i^2 \nabla \varepsilon + q_V \mathbf{E}_i. \quad (4)$$

Where, $q_V = \nabla \cdot (\varepsilon_0 \varepsilon \mathbf{E}_i)$ is called the charge density and $\nabla\varepsilon$ is the gradient of the dielectric constant across the interface. The term q_V can also be expressed as, $\varepsilon_0(\sigma \mathbf{E}_i) \cdot \nabla(\varepsilon/\sigma)$, after some algebraic rearrangements.
We employed phase field method to track the interface.[72] The transport equation for this phase field parameter (ϕ) is,

$$\dot{\phi} + \mathbf{u}_i \cdot \nabla\phi = \nabla \cdot \chi(\nabla G). \quad (5)$$

The parameter ϕ acquires a value of -1 in water and 1 in oil. The variable χ captures the mobility of the interface and the chemical potential is $G = F'(\phi) = \lambda[-\nabla^2\phi + \phi(\phi^2 - 1)N^2$. The chemical potential is evaluated in terms of the free energy functional, $F(\phi)$,as,

$$F(\phi) = \int_\Omega f_{tot}\, d\Omega = \int_\Omega \left(f(\phi) + \frac{1}{2}\lambda |\nabla^2 \phi| \right) d\Omega. \quad (6)$$

In Equation (6), Ω is the volume of the computational domain and f_{tot} is the total free energy density, which is the sum of the bulk energy or double well potential $[f(\phi) = \lambda/4N^2(\phi^2 - 1)^2]$ and the surface energy. The mixing energy density is expressed as, $\lambda = (3\gamma N)/(2\sqrt{2})$, in which γ and N are the interfacial tension and thickness of the diffused interface. The

interfacial density (ρ), viscosity (η), permittivity (ε), and conductivity (σ), are evaluated in terms of ϕ with the help of following rule, $a = 0.5[a_1(1+\phi) + a_2(1-\phi)]$, where a can be any of ρ, η, ε, and σ.

The normal inflow velocity ($\mathbf{v}_i = U$) boundary condition has been enforced at the inlets of the fluids and at the outlet, default pressure with zero viscous stress boundary condition has been enforced. The channel walls are considered to be wetting, non-slipping, and impermeable. The equilibrium contact angle (θ) of an oil droplet resting on the channel wall and embedded inside a water medium is set to 45° in the entire study. Constant voltage boundary conditions have been enforced at the anode ($V_i = V_0$) and cathode ($V_i = 0$).

2.2 Solution Methodology

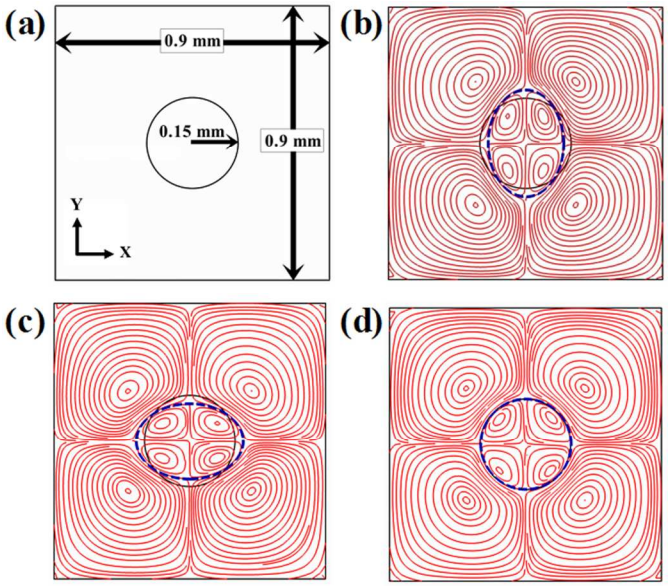

Figure 2. Leaky dielectric droplet of diameter 0.3 mm is deforming under a direct current (DC) electric field when the applied potential is 988 V.[75] Image (a) schematically shows the computational domain. Image (b) shows the deformation of circular droplet into a prolate shape when E_r = 0.5 and S_r = 5. Image (c) shows the droplet deformation to an oblate shape when E_r = 60 and S_r = 5. Image (d) shows that when E_r = 10 and S_r = 5 the droplet remains undeformed. Images (b), (c) and (d) are observed at, t = 0.032 s. The other parameters employed for this study are, ρ_r = 1, η_r = 10, and γ = 5.8 mNm^{-1}.

Figure 1 shows the two-dimensional (2-D) microchannel of diameter (d_c) 100 µm and length 1.45 mm. The 50 µm wide electrodes at the 200 µm downstream of the T-junctionl generate the AC electrostatic field. Grid independent solutions have been achieved when ~7500 quadrilateral elements are laid down in the computational domain. The COMSOL™ multi-physics software has been used to solve the unsteady governing equations (1) and (2) along with the boundary conditions. The software employs the Galerkin least-square finite element method to discretize the convective-diffusion equations. The numerical stabilization of this solver has been achieved by employing the streamline and crosswind diffusions alongside using the second order elements for velocity and first order elements for pressure gradient calculations. The velocity and pressure profiles for the flow have been obtained by incremental pressure correction for the segregated predictor-corrector method. The backward Euler scheme and the second-order backward difference method are used for consistent initialization, time-marching, and error minimization. The average time step size has been observed to be ~10^{-4} s for the converged solutions.

Previous studies have shown that a jump in the EHD stress across the liquid-liquid interface can lead to interesting shapes. For example, Lin *et al.*[75] have shown that when both the fluids are leaky dielectric, a spherical droplet can deform into a prolate or an oblate shaped spheroid under the influence of an external electric field based upon the ratio of the dielectric constants, $E_r = E_{dispersed}/E_{medium}$, and the ratio of the conductivity, $S_r = S_{dispersed}/S_{medium}$ of the fluids. **Figure 2** shows the typical geometry for validating the results from the literature for the geometry shown in the image (a).[75] **Figure 2(b)** shows that a perfectly round droplet deforms into prolate shape when E_r = 0.5 and S_r = 5, whereas **Figure 2(c)** show that the same droplet under exactly the same conditions deforms into an oblate shape when E_r = 60 and S_r = 5. However, for E_r = 10 and S_r = 5 almost no deformation was observed as can be seen in the **Figure 2(d)**. Concisely, Figure 2 confirms the accuracy of the software used in this work in simulating the EHD multi-physics employing the two-phase systems.

3. Results and discussion

The pressure-driven multiphase flows inside the microchannels can lead to stratified, slug, plug, droplet, or core-annular flow morphologies with the variations in the flow ratios of the phases at the inlet. In such cases, it is now well understood that the droplet flow patterns appear only for a specific window of flow ratios of the incoming phases.[30,33,42,47] Over a period of time, this particular aspect has limited the usefulness of the pressure-driven droplet microfluidics for different kinds of applications. Certainly, a more desirable situation is to have droplet flow patterns for the full range of inlet flow rates of the phases. In this direction, application of the external fields can be simple and efficient alternative, which can convert any type of the pressure-driven flow patterns into droplets.[7,62,70,79] Transformation of other flow patterns into droplets not only increases surface to volume ratio for larger mass, heat, or momentum transfer, but also helps in developing miniaturized devices with a higher throughput because the droplets pass through the channels at a much faster rate.[80-82] In the present study, we employ a simple non-invasive strategy to produce droplets inside a 'T' shaped microchannel with the help of a localized alternating current (AC) electric field. It may be noted here that all the ratios reported for the physical or flow properties (ρ_r, ε_r, η_r, σ_r, and Q) are considered as, $a_r = a_1/a_2$, where a can be any of ρ, η, ε, and σ. The typical values employed in the simulations for the physical properties of oil and water are, ε_r = 2.2/80 = 0.0275, η_r = 0.01 Pas /0.001 Pas = 10, σ_r = 4×10^{-6} Sm^{-1}/10^{-3} Sm^{-1} = 0.004, ρ_r = 1000 kgm^{-3}/1000 kgm^{-3} = 1, and $Q = v_1/v_2$ = 0.1.

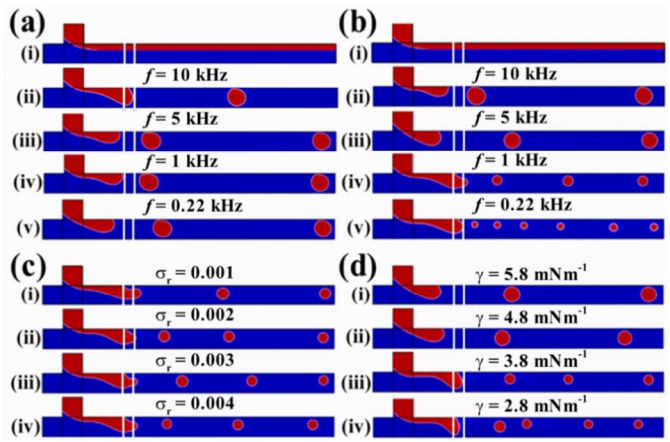

Figure 3. Image sets (a) and (b) shows the variation in the flow morphologies with the frequency (f) of the applied AC voltage for purely dielectric and leaky dielectric fluids, respectively. In both the image sets the frame (i) shows the steady state pressure-driven flow pattern whereas the frames (ii) – (v) the flow morphologies at steady state with the AC field. Image sets (c) and (d) shows the change in the flow patterns with the conductivity ratio (σ_r) and interfacial tension (γ). Other parameters taken for this study are, γ = 5.8 mNm^{-1} (image sets a, b, and c), θ = 45°, ε_r = 0.0275, ρ_r = 1, η_r = 10, σ_r = 0.004 (image sets b and d), Ψ = 3 MVm^{-1}, and Q = 0.1. The frequency (f) of the applied AC voltage for the image sets (c) and (d) are 1 kHz and 5 kHz, respectively. The darker-blue (lighter-red) shade shows the water (oil) phase.

Figure 3 shows a few cases where an externally applied AC filed breaks down a pressure driven flow pattern into droplets. **Figures 3(a)** and **3(b)** show the influence of frequency (f) of the applied AC electric field when the phases are purely dielectric and weakly conducting, respectively. Frame (i) in these two image sets show the steady-state pressure-driven flow patterns when water (oil) enters horizontally (vertically) inside the channel. In general, we employed sinusoidal waveform in the simulations for the AC field unless mentioned otherwise. Frame (ii) in these images show that under the influence of a localized AC electric field the stratified flow patterns can transform to droplets at a peak voltage of 150 V with f = 10 kHz. The system shown in this frame resembles the configuration shown in the **Figure 2(b)** where a liquid droplet with lower dielectric permittivity and higher electrical conductivity is exposed to an external electrostatic field inside a medium of higher dielectric permittivity and lower electrical conductivity. Frame (ii) in **Figure 3(a)** shows that, in such a situation, the dielectrophoretic force (F_{DEP}) at the interface originating from the external AC field elongates the oil phase vertically in the y-direction to form an 'oil plug' at the zone where the electrodes are placed. In consequence, the elongated oil-phase experiences a thrust from the inlet flows, which helps in producing the droplets. The droplet pinches out off the mainstream due to the collective destabilizing influences originating from the stresses due to the external AC electric field and the capillary force, undergoing Rayleigh instability.

Importantly, the frames (iii) – (v) in the **Figure 3(a)** show that when both the fluids are purely dielectric ($\sigma_1 = \sigma_2 = 0$, ε_1 = 2.2 and ε_2 = 80) the flow pattern remains almost unaltered as f is progressively reduced from 10 kHz to 0.22 kHz. In contrast, when the fluids are considered to be weakly conducting (ε_1 = 2.2, ε_2 = 80, σ_1 = 4×10^{-6} S/m, and σ_2 = 10^{-3} S/m) in **Figure 3(b)**, frames (ii) – (v) show a progressive reduction in droplet size and increase in f from 10 kHz to 0.22 kHz. Further, **Figure 3(c)** and **3(d)** depict the flow morphologies with the variation in the conductivity ratio of oil to water ($\sigma_r = \sigma_1/\sigma_2$) and oil-water interfacial tension (γ), respectively. The frames (i) – (iv) in the **Figure 3(c)** depict that the increase in σ_r can enhance the EHD stress across the interface to reduce the droplet size inside the channel. The frames (i) – (iv) in the **Figure 3(d)** show that the reduction in γ can cause a net reduction in the stabilizing influence at the interface, which can enforce drop formation much more easily. Concisely, the **Figure 3** shows a simple method to transform a pressure-driven stratified flow into droplets under the influence of an external AC electric field.

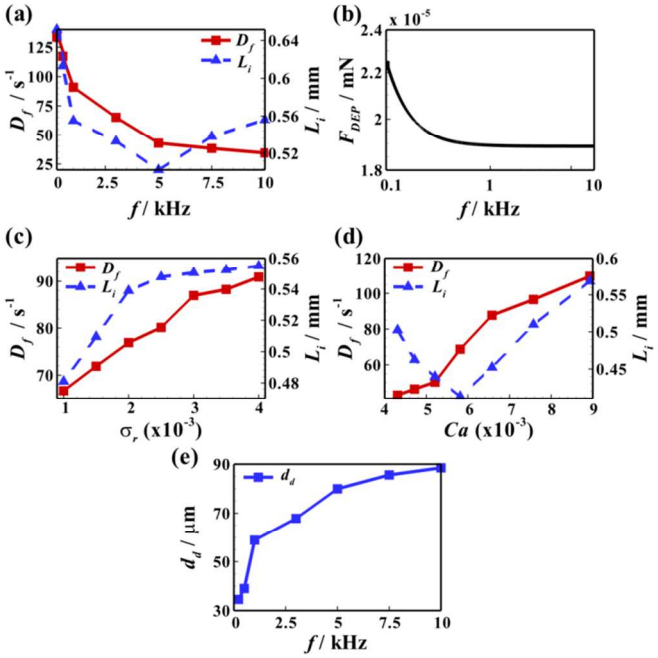

Figure 4. The plot (a) shows the variation in interfacial contact length (L_i – right side of y-axis) and the frequency (D_f – left side of y-axis) of the flow patterns passing through the outlet when the frequency (f) of the applied AC electric field is altered. The plot (b) shows the variation of the dielectrophorectic force (F_{DEP}) acting on a spherical liquid droplet of diameter 80 μm surrounded by conducting dielectric medium inside the electrode region with the variation of frequency (f) of the applied AC electric field. Plot (c) shows the variation in L_i (right side of y-axis) and D_f (left side of y-axis) with σ_r for an AC voltage with frequency of f = 1 KHz. Plot (d) shows the variation in L_i (right side of y-axis) and D_f (left side of y-axis) with capillary number (Ca) for an AC voltage with frequency of f = 5 KHz. Plot (e) shows the variation of droplet diameter (d_d) with the frequency (f) of the applied AC voltage. The other parameters employed for the plots are, Ψ = 3 MVm^{-1}, θ = 45°, σ_r = 0.004 (plots a, b, d and e), γ = 5.8 mNm^{-1} (plots a, b, c and e), ε_r = 0.0275, ρ_r = 1, η_r = 10, and Q = 0.1.

Figure 4 shows the sensitivity of with f, σ_r, and capillary number (Ca) reported in **Figure 3** on the surface to volume ratio and the throughput of the flow patterns. Here $Ca = \mu_1 u_1/\gamma$ is defined for the dispersed oil phase in which u_1 = 0.025ms^{-1}, is the oil velocity at the inlet. In these plots, the cumulative length of the interfacial contact between oil and water (L_i – triangular symbols, broken line, plotted in the right y-axis) is a measure of the total available interface for heat or mass or momentum

exchange. The frequency of the flow patterns at the outlet (D_f – square symbols, solid line, plotted in the left *y*-axis) is a measure of the throughput. The parameter L_i is calculated as the total length of the oil-water interface at the downstream of the electrodes, which is equal to the product of the number of droplets (or flow features) at the downstream of the electrodes with the perimeter of each droplet (or flow feature). **Figure 4(a)** shows that D_f increases significantly with reduction in f whereas, L_i initially reduces and then increases with the reduction in f below 5 kHz. The variation in the droplet size with f can be explained through a simple correlation shown below, which corresponds to the variation of the dielectrophoretic force (F_{DEP}) on a spherical drop of radius r when exposed to an external AC electric field.[83]

$$\langle F_{DEP} \rangle = 2\pi r^3 \varepsilon_m \mathrm{Re}\left\{\frac{\varepsilon_p^* - \varepsilon_m^*}{\varepsilon_p^* + 2\varepsilon_m^*}\right\} \nabla \left|\vec{E}_{rms}\right|^2. \qquad (7)$$

Here the notations ε_p^* and ε_m^* are the complex permittivities of the droplet and the surrounding medium and the complex dielectric constant is defined as, $\varepsilon^* = \varepsilon + (i\sigma/f)$. Here ε is the dielectric constant, σ is the electrical conductivity, f is the field frequency, Re denotes the real part of the variable, and i denotes the imaginary unit. **Figure 4(b)** shows the F_{DEP} acting on the interface of a droplet due to applied the AC field is larger when f is lower. Thus, for the system considered in the present study, it can easily be envisaged that, in the region where the electrodes are placed, a larger F_{DEP} at the interface originating from a lower f is responsible for creating the droplets of smaller size and higher frequency. The changeover of the droplet size and frequency with f has already been depicted in the frames (ii) – (v) in the **Figure 3(b)**. **Figure 4(c)** shows that D_f and L_i both increase with an increase in the conductivity ratio σ_r of the fluids. Again, a larger F_{DEP} with increase in σ_r causes the reduction in the droplet size and increase in its frequency. **Figure 4(d)** shows that with increase in the magnitude of Ca (decrease in γ) the stabilizing influence at the interface weakens against the destabilizing electric field force. This leads to the formation of smaller droplets and increment in both L_i and D_f. Further, **Figure 4(e)** shows that with increase in AC frequency the size of the droplet reduces owing to the reduction in F_{DEP}, as shown in the **Figure 4b**. This is also evident from equation (7) that the complex permittivity decreases with increase in f, which eventually lowers the F_{DEP} to create droplets of bigger size.

Figure 5 shows the influence of the different waveforms of the AC electric field on the pressure-driven flow morphologies. For this purpose, four different types, namely, sine, saw-tooth, smoothed square, and triangular waveforms are chosen, as shown in the images (a) – (d) in the column I of **Figure 5**. The figure suggests that at a peak voltage of 150 V and frequency of 5 kHz, the droplet size and frequency can be tuned simply by changing the waveform of the AC field. The flow morphologies in the images (a) – (d) of the column II of **Figure 5** suggest that with the variation in the waveform the droplet size can reduce drastically. The drop size is found to be almost 5 times smaller in the triangular waveform as compared to the sine waveform, as shown in the images (a) and (d). Column III in the **Figure 5** shows the oil-water interface (the solid lines) near the electrode region in which the grayscale contours show the magnitudes of the electric field force per unit volume (MNm^{-3}) because of the electric field.

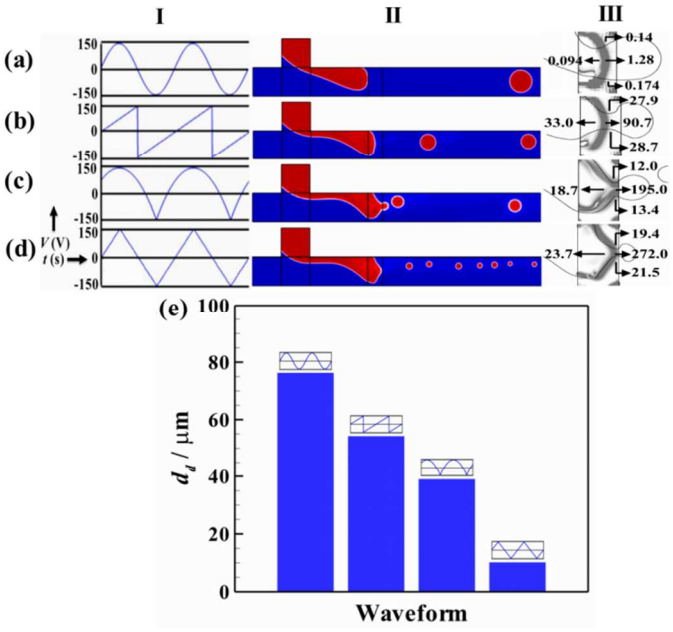

Figure 5. Images (a) – (d) correspond to the sinusoidal, saw-tooth, smoothed square and triangular waveforms, as shown in the column I. Column II shows the change in the flow morphologies with the variation in the waveform. Column III shows the oil-water interface (the lines) near the electrode region in which the grayscale contours show the magnitudes of the force because of the electric field from the simulations. Darker shades in the grayscale indicate a region with higher force. The numbers on the images show some typical magnitudes of the force in MNm^{-3} in the locations where the tail of the arrowheads are situated. Plot (e) shows the variation in droplet diameter (d_d) with different AC waveforms. The corresponding waveforms are shown above its respective bars. Other parameters employed for the plots are, θ = 45°, ε_r = 0.0275, η_r = 10, ρ_r = 1, σ_r = 0.004, Ψ = 3 MVm^{-1}, f = 5 kHz, and Q = 0.1. The darker-blue (lighter-red) shade shows the water (oil) phase.

It may be noted here that the divergence of the Maxwell's stress tensor, as shown in the Equation (4), provides the total electric field force per unit volume at a particular location inside the electrode region. The typical values of the electric field force in the column III of **Figure 5** are calculated by computing the *x*- and *y*-directional components of the total electric field force per unit volume from the simulations. Darker shades in the grayscale indicate a region with higher electric field force per unit volume. The numbers on the images show some typical magnitudes of the electric field force per unit volume in the locations where the tail of the arrowheads are situated. The contour and the magnitudes of the electric field force per unit volume suggest that the difference in the horizontal component (*x*-direction) of the electric field force per unit volume near the pinch off zone increases with the change in the waveform. For example, in the sinusoidal waveform in the image (a) the difference is around 1.186 MNm^{-3} (1.28 MNm^{-3} – 0.094 MNm^{-3}) whereas for the triangular waveform the difference increases

to 248.3 MNm^{-3} (272 MNm^{-3} – 23.7 MNm^{-3}). In comparison, the difference in the magnitude of the vertical component (*y*-direction) of the electric field force per unit volume near the pinch off zone remains minimal in all the cases although the magnitude changes considerably with the waveform. The force contours suggest that the significant variation in the horizontal component (*x*-direction) of the electric field force per unit volume near the pinch off zone is responsible for the variation in the size of the droplet with the waveform of the AC field. **Figure 5(e)** shows the variation of droplet diameter (d_d) with applied AC waveforms. The plot clearly suggests that the droplet diameter decreases as the waveforms are changed. The change in the droplet size with waveforms can be attributed to the variation in the corresponding F_{DEP}, as shown in the contour plots of the column III.

4. Conclusions

The dielectrophoretic forces originating from the externally applied AC electric field deforms the interface of a pair of weakly conducting liquids to engender droplet flow patterns inside microchannels. The present study shows that size, shape, and frequency of the droplets are functions of the frequency and waveform of the AC field. The variation in the electric field stress at the interface with the frequency and waveform of the AC field facilitates the formation of droplets with smaller size and higher throughput. The variation in the frequency and the waveform of the AC electric field are found to be more effective in generating the droplets when both the liquids are weakly conducting than when they are purely dielectric in nature. Since the reported field intensities are of rather moderate in magnitude, the flow patterns are expected to be even smaller with increase in the applied field intensity. The proposed non-invasive pathway to digitize the flow patterns inside a multiphase microfluidic device can help in the development of next-generation microfluidic devices of smaller size and higher throughput.

Acknowledgements

The authors gratefully acknowledge the financial supports from DST-SERB - grant no. SR/S3/CE/0079/2010, DST-FIST - grant no. SR/FST/ETII-028/2010, and DeitY - grant no. 5(9)/2012-NANO.

Notes and references

[a]Department of Chemical Engineering, Indian Institute of Technology Guwahati, India.

[b]Centre for Nanotechnology, Indian Institute of Technology Guwahati, India.

*Corresponding author: Tel-+913612582254, Email:dipban@iitg.ernet.in.

1 M. Nakano, N. Nakai, H. Kurita, J. Komatsu, K. Takashima, S. Katsura and A. Mizuno, *Journal of Bioscience and Bioengineering*, 2005, **99**, 293.

2 V. Taly, D. Pekin, A. E. Abed and P. Laurent-Puig, *Trends in Molecular Medicine*, 2012, **18**, 405.

3 U. Lehmann, D. de Courten, C. Vandevyver, V. K. Parashar and M. A. M. Gijs, *Microelectronic Engineering*, 2007, **84**, 1669.

4 H. Tsuchiya, M. Okochi, N. Nagao, M. Shikida and H. Honda, *Sensors and Actuators B: Chemical*, 2008, **130**, 583.

5 M. Vojtíšek, A. Iles and N. Pamme, *Biosensors and Bioelectronics*, 2010, **25**, 2172.

6 C. Zhang, J. Xu, W. Ma and W. Zheng, *Biotechnology Advances*, 2006, **24**, 243.

7 S. H. Tan, B. Semin and J.-C. Baret, *Lab on a Chip*, 2014, **14**, 1099.

8 S. H. Tan, F. Maes, B. Semin, J. Vrignon and J.-C. Baret, *Sci. Rep.*, 2014, **4**, 4787.

9 V. R. Regatte and N. S. Kaisare, *Chemical Engineering Journal*, 2013, **215–216**, 876.

10 T. Salmi, J. H. Carucci, M. Roche, K. Eränen, J. Wärnå and D. Murzin, *Chemical Engineering Science*, 2013, **87**, 306.

11 D. Wlodkowic and J. M. Cooper, *Anal Bioanal Chem*, 2010, **398**, 193.

12 K. S. Krishna, Y. Li, S. Li and C. S. S. R. Kumar, *Advanced Drug Delivery Reviews*, 2013, **65**, 1470.

13 L. Capretto, D. Carugo, S. Mazzitelli, C. Nastruzzi and X. Zhang, *Advanced Drug Delivery Reviews*, 2013, **65**, 1496.

14 D. Bennet and S. Kim, *Journal of Materials Science*, 2011, **46**, 4723.

15 P. Song, R. Hu, D. J. H. Tng and K.-T. Yong, *RSC Advances*, 2014, **4**, 11499.

16 A. Babu, A. K. Templeton, A. Munshi and R. Ramesh, *AAPS PharmSciTech*, 2014, **15**, 709.

17 J. R. Burns and C. Ramshaw, *Lab on a Chip*, 2001, **1**, 10.

18 B. Ahmed, D. Barrow and T. Wirth, *Advanced Synthesis & Catalysis*, 2006, **348**, 1043.

19 D. Bothe, C. Stemich and H.-J. Warnecke, *Chemical Engineering Science*, 2006, **61**, 2950.

20 A. A. Alexeenko, D. A. Fedosov, S. F. Gimelshein, D. A. Levin and R. J. Collins, *Journal of Microelectromechanical Systems,* 2006, **15**, 181.

21 W.-Y. Lin, Y. Wang, S. Wang and H.-R. Tseng, *Nano Today*, 2009, **4**, 470.

22 B. Buonomo and O. Manca, *International Journal of Thermal Sciences*, 2012, **56**, 35.

23 H. Gau, S. Herminghaus, P. Lenz and R. Lipowsky, *Science*, 1999, **283**, 46.

24 B. Zhao, J. S. Moore and D. J. Beebe, *Science*, 2001, **291**, 1023.

25 J. Judy, D. Maynes and B. W. Webb, *International Journal of Heat and Mass Transfer*, 2002, **45**, 3477.

26 J. Ou, B. Perot and J. P. Rothstein, *Physics of Fluids*, 2004, **16**, 4635.

27 A. Günther and K. F. Jensen, *Lab on a Chip*, 2006, **6**, 1487.

28 D. Di Carlo, *Lab on a Chip*, 2009, **9**, 3038.

29 S. L. Anna, N. Bontoux and H. A. Stone, *Applied Physics Letters*, 2003, **82**, 364.

30 P. Garstecki, M. J. Fuerstman, H. A. Stone and G. M. Whitesides, *Lab on a Chip*, 2006, **6**, 437.

31 T. Cubaud and T. G. Mason, *Physical Review Letters*, 2006, **96**, 114501.

32 T. Cubaud and T. G. Mason, *Physical Review Letters*, 2007, **98**, 264501.

33 T. Cubaud and T. G. Mason, *Physics of Fluids*, 2008, **20**, 053302.

34 T. Thorsen, R. W. Roberts, F. H. Arnold and S. R. Quake, *Physical Review Letters*, 2001, **86**, 4163.
35 J. D. Tice, H. Song, A. D. Lyon and R. F. Ismagilov, *Langmuir*, 2003, **19**, 9127.
36 M. Yamada, S. Doi, H. Maenaka, M. Yasuda and M. Seki, *J Colloid Interface Sci*, 2008, **321**, 401.
37 H. A. Stone, A. D. Stroock and A. Ajdari, *Annual Review of Fluid Mechanics*, 2004, **36**, 381.
38 L. Shui, J. C. T. Eijkel and A. van den Berg, *Adv Colloid Interface Sci*, 2007, **133**, 35.
39 S. Ghosh, T. K. Mandal, G. Das and P. K. Das, *Renewable and Sustainable Energy Reviews*, 2009, **13**, 1957.
40 C. N. Baroud, F. Gallaire and R. Dangla, *Lab on a Chip*, 2010, **10**, 2032.
41 V. Kumar, M. Paraschivoiu and K. D. P. Nigam, *Chemical Engineering Science*, 2011, **66**, 1329.
42 C.-X. Zhao and A. P. J. Middelberg, *Chemical Engineering Science*, 2011, **66**, 1394.
43 K. A. Triplett, S. M. Ghiaasiaan, S. I. Abdel-Khalik and D. L. Sadowski, *International Journal of Multiphase Flow*, 1999, **25**, 377.
44 A. Kawahara, P. M.-Y. Chung and M. Kawaji, *International Journal of Multiphase Flow*, 2002, **28**, 1411.
45 P. M.-Y. Chung, M. Kawaji, A. Kawahara and Y. Shibata, *Journal of Fluids Engineering*, 2004, **126**, 546.
46 P. M.-Y. Chung and M. Kawaji, *International Journal of Multiphase Flow*, 2004, **30**, 735.
47 R. M. Santos and M. Kawaji, *International Journal of Multiphase Flow*, 2010, **36**, 314.
48 T. S. Fouilland, D. F. Fletcher and B. S. Haynes, *Chemical Engineering Science*, 2010, **65**, 5344.
49 D. R. Webster and E. K. Longmire, *Experiments in Fluids*, 2001, **30**, 47.
50 A.-L. Dessimoz, L. Cavin, A. Renken and L. Kiwi-Minsker, *Chemical Engineering Science*, 2008, **63**, 4035.
51 J. Jovanović, W. Zhou, E. V. Rebrov, T. A. Nijhuis, V. Hessel and J. C. Schouten, *Chemical Engineering Science*, 2011, **66**, 42.
52 T.-S. Leu, C.-T. Wang and J.-M. Sun, *Journal of Mechanics*, 2010, **26**, 259.
53 S. Lecuyer, W. D. Ristenpart, O. Vincent and H. A. Stone, *Applied Physics Letters*, 2008, **92**, 104105.
54 S. Laohalertdecha and S. Wongwises, *Experimental Thermal and Fluid Science*, 2006, **30**, 675.
55 P. D. S. Reddy, D. Bandyopadhyay and A. Sharma, *The Journal of Physical Chemistry C*, 2010, **114**, 21020.
56 P. D. S. Reddy, D. Bandyopadhyay, S. W. Joo, A. Sharma and S. Qian, *Physical Review E*, 2011, **83**, 036313.
57 B. Ray, P. D. S. Reddy, D. Bandyopadhyay, S. W. Joo, A. Sharma, S. Qian and G. Biswas, *Electrophoresis*, 2011, **32**, 3257.
58 B. Ray, P. D. S. Reddy, D. Bandyopadhyay, S. W. Joo, A. Sharma, S. Qian and G. Biswas, *Theoretical and Computational Fluid Dynamics*, 2011, **26**, 311.
59 D. Bandyopadhyay, P. D. S. Reddy, A. Sharma, S. W. Joo and S. Qian, *Theoretical and Computational Fluid Dynamics*, 2012, **26**, 23.
60 S. Torza, R. G. Cox and S. G. Mason, *Philosophical Transactions of the Royal Society A: Mathematical, Physical and Engineering Sciences*, 1971, **269**, 295.
61 O. Vizika and D. A. Saville, *Journal of Fluid Mechanics*, 1992, **239**, 1.
62 M. Sato, S. Kato and M. Saito, *IEEE Transactions on Industry Applications*, 1996, **32**, 138.
63 P. Singh and N. Aubry, *Electrophoresis*, 2007, **28**, 644.
64 J. D. Sherwood, *Journal of Fluid Mechanics*, 1988, **188**, 133
65 J. Q. Feng and T. C. Scott, *Journal of Fluid Mechanics*, 1996, **311**, 289.
66 J. Hua, L. K. Lim and C.-H. Wang, *Physics of Fluids*, 2008, **20**, 113302.
67 J. M. López-Herrera, S. Popinet and M. A. Herrada, *Journal of Computational Physics*, 2011, **230**, 1939.
68 A. Fernández, G. Tryggvason, J. Che and S. L. Ceccio, *Physics of Fluids*, 2005, **17**, 093302.
69 J. Zhang and D. Y. Kwok, *Journal of Computational Physics*, 2005, **206**, 150.
70 O. Ozen, N. Aubry, D. T. Papageorgiou and P. G. Petropoulos, *Physical Review Letters*, 2006, **96**, 144501.
71 D. M. Anderson, G. B. McFadden and A. A. Wheeler, *Annual Review of Fluid Mechanics*, 1998, **30**, 139.
72 D. Jacqmin, *Journal of Computational Physics*, 1999, **155**, 96.
73 V. E. Badalassi, H. D. Ceniceros and S. Banerjee, *Journal of Computational Physics*, 2003, **190**, 371.
74 X. Yang, J. J. Feng, C. Liu and J. Shen, *Journal of Computational Physics*, 2006, **218**, 417.
75 Y. Lin, P. Skjetne and A. Carlson, *International Journal of Multiphase Flow*, 2012, **45**, 1.
76 M. Plapp, *Philosophical Magazine*, 2011, **91**, 25.
77 I. Steinbach, L. Zhang and M. Plapp, *Acta Materialia*, 2012, **60**, 2689.
78 P. Yue, C. Zhou, J. J. Feng, C. F. Ollivier-Gooch and H. H. Hu, *Journal of Computational Physics*, 2006, **219**, 47.
79 A. Sharma, V. Tiwari, V. Kumar, T. K. Mandal, D. Bandyopadhyay, *Electrophoresis,* 2014, **35**, 2930-2937.
80 C. Zhang and D. Xing, *Nucleic Acids Research*, 2007, **35**, 4223.
81 K.-Y. Lien and G.-B. Lee, *Analyst*, 2010, **135**, 1499.
82 L. D. Garza-Garcia, L. M. Carrillo-Cocom, D. Araiz-Hernandez, P. Soto-Vazquez, J. Lopez-Meza, E. J. Tapia-Mejia, S. Camacho-Leon, E. Garcia-Lopez, C. A. Rodriguez-Gonzalez and M. M. Alvarez, *Lab on a Chip*, 2013, **13**, 1243.
83 H. A. Pohl, *Dielectrophoresis: the behavior of neutral matter in nonuniform electric fields*, ed. M. M. Woolfson and J. M. Ziman, Cambridge University Press. Cambridge, 1978, vol. 80.